

Optimizing Levitation Devices for Wireless Power Transfer: An Fe-NCS Grid Structure Approach

Fengxian Wang , Qingxin Yang, Xian Zhang , Zhaoyang Yuan , Member, IEEE, and Xuejing Ni

Abstract—This article proposes a solution for driving a microdisplacement device in the coupling space of a wireless power transfer system. The solution involves using a levitation device made of a combination of Fe-based nanocrystalline alloys (Fe-NCS) and aluminium. The dynamic model of the levitation device is analyzed to understand the electromagnetic force involved, and an optimized grid-type Fe-NCS structure is proposed to reduce the weight of the device and achieve stable levitation. The optimization uses a variable acceleration particle swarm optimization algorithm. A 3.7-kW prototype with 100-A input current is built to validate the proposed structure, and the results show that the optimized grid-type structure effectively enhances the average horizontal velocity of the levitation drive to 9.3 cm/s.

Index Terms—Electromagnetic force (EMF), grid-type structure, levitation device, particle swarm optimization (PSO), wireless power transfer (WPT).

I. INTRODUCTION

WIRELESS power transfer (WPT) technology transmits energy efficiently through the near-zone electromagnetic field excited by the high-frequency resonant current flowing in the coupled coils [1], [2], [3], [4]. According to the electrodynamics theory, the alternating electromagnetic field excited by the WPT system will generate a force on the charged particles in the coupling space [5], [6], [7], [8]. Using this force to control the microdisplacement device and realize the efficient transfer of power at the same time is one of the research hotspots of the WPT technology [9], [10], [11].

Some scholars and research institutions have carried out many research works on the electromagnetic force (EMF) of WPT

Manuscript received 3 April 2023; revised 27 June 2023; accepted 10 July 2023. Date of publication 18 July 2023; date of current version 1 September 2023. This work was supported in part by the National Natural Science Foundation of China under Projects 51977147 and 52122701, in part by the Key Program of Natural Science Foundation of Tianjin under Grant 22JCZDJC00620, and in part by the Interdisciplinary postgraduate Training Program of Hebei University of Technology under Grant HEBUT-Y-XKJC-2022109. Recommended for publication by Associate Editor M. Liu (*Corresponding author: Xian Zhang*.)

Fengxian Wang, Xian Zhang, and Zhaoyang Yuan are with the State Key Laboratory of Reliability and Intelligence of Electrical Equipment, Hebei University of Technology, Tianjin 300401, China (e-mail: fx-wang@outlook.com; zhangxian@hebut.edu.cn; zyuan@ieee.org).

Qingxin Yang is with the Tianjin University of Technology, Tianjin 300384, China (e-mail: qxyang@tjut.edu.cn).

Xuejing Ni is with the GD Power Shuangwei Inner Mongolia Shang-haimiao Energy Company, Ltd., Inner Mongolia 017000, China (e-mail: nxj838435084@163.com).

Color versions of one or more figures in this article are available at <https://doi.org/10.1109/TPEL.2023.3296521>.

Digital Object Identifier 10.1109/TPEL.2023.3296521

systems. In [12] and [13], Kim et al. proposed a microrobot displacement device which realizes 2-D directional motion driven by EMF while realizing wireless power transfer. To realize the 3-D steering motion of the microrobot, the three mutually orthogonal Helmholtz coils are proposed, which can generate a uniform electromagnetic field in the 3-D space [14]. Oka and Tanaka [15] designed a novel magnetic levitation device to levitate the receiver mechanism by the electromagnetic repulsion provided by the coupled coils and the permanent magnet. Liu et al. [16] designed a novel magnetic resonant coupling motor without any iron or permanent magnet core. The rotor is rotated by the multidirectional electromagnetic torque adjusted by the excitation frequency that follows the trajectory of resonant frequency splitting. To reduce the potential hazard to the safe operation of the system caused by the EMF on the coupler, Wang et al. [17] proposed a smoothing method based on the phase difference control, which can minimize the combined EMF on the coupler. The research on the EMF of the WPT system is mainly to meet the specific driving requirements of microminiature robots in the coupling space and to suppress the EMF on the coupler. The specific application scenarios include implantable medical devices, microrobots used for hazardous operations, etc. The current research mainly focuses on the precise navigation of the driving body, multidimensional driving under multiple driving coils, multigroup omnidirectional driving control, and spatial directional control. There is no report on the mechanical performance and dynamic characteristics of different material combinations.

Using EMFs to attain precise motion states in levitation devices is a highly regarded research area. In contrast, there are existing literature reports in other electromagnetic contexts, such as biomedical and microrobotics domains, the specific problem of levitation devices in WPT centers on achieving desired motion states within the electromagnetic coupling space [18], [19], [20], [21]. This sets it apart from levitation device challenges encountered in other fields and necessitates careful design and optimization to meet the distinctive demands of energy transmission.

This article focuses on driving the levitation device while transferring the power in the WPT system. It is necessary to state that, unlike the traditional focus on the loss of metallic foreign bodies in the coupling space, this article is more concerned with its force and motion characteristics and achieving stable levitation and rapid moving motion with the characteristics. Based on the difference in the EMF between the Fe-based nanocrystalline alloys (Fe-NCS) and the aluminium, a

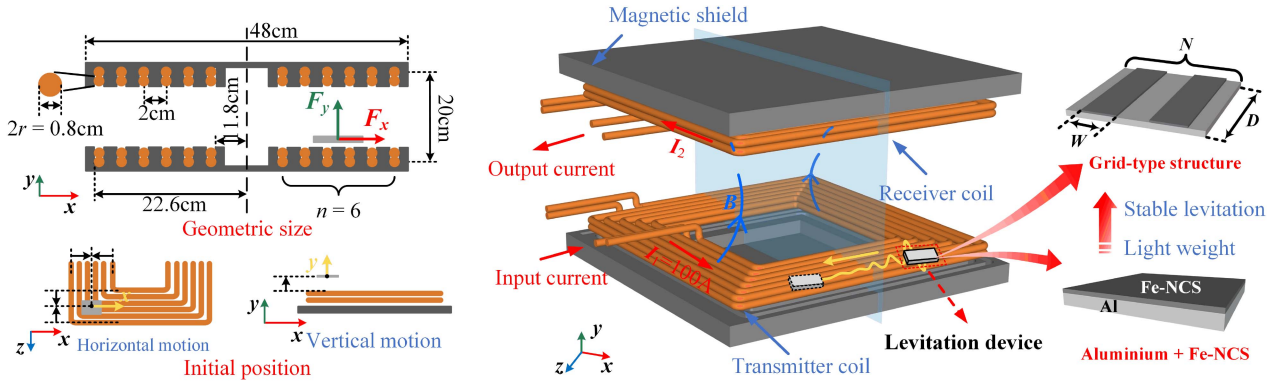


Fig. 1. Schematic diagram of the levitation device consisting of the Fe-NCS and the aluminium.

levitation device consisting of the two materials is proposed. In Section I, the mechanism of the EMF on the levitation device in the coupling space is studied. The motion characteristics of the proposed levitation device are investigated. To reduce the weight of the levitation device and achieve stable levitation, the optimized levitation device with the grid-type Fe-NCS structure is proposed based on the variable acceleration particle swarm optimization (VA-PSO) algorithm in Section II. In Section III, a prototype is built to verify the accuracy of the optimized design results. Finally, Section IV concludes this article.

II. LEVITATION DEVICE CONSISTING OF THE FE-NCS AND THE ALUMINIUM

Considering the weight of the levitation device, Fe-NCS with light mass and good magnetism is used in this article after fragmentation treatment. It has a relative permeability μ_r of 600 and operates in a nonsaturated state. Affected by the alternating electromagnetic field in the coupling space, the aluminium generates multiple concentrically distributed rings of induced currents due to the eddy current effect. At the same time, the Fe-NCS generate molecular magnetization currents due to the magnetization effect, according to the different force performance of these two types of materials. This article proposes a levitation device consisting of Fe-NCS and aluminium.

The schematic diagram of the levitation device is shown in Fig. 1. The levitation device will generate an additional electromagnetic field and distort the original field strength distribution after the eddy current and magnetization effects. In particular, the WPT system usually treats aluminium in the coupling space as a foreign body, which can harm the system when it is in the working system for a long time. However, the aluminium in the coupling space has motion characteristics due to EMF and loss characteristics. This article does not focus on its loss characteristics but uses its dynamic characteristics to achieve specific requirements. This article chooses the SS-type topology as the primary circuit configuration. Fig. 2(a) is the topology of the WPT system, and the current-type inverter circuit is chosen as the excitation for the coils.

As depicted in Fig. 2(b), the schematic representation of the equivalent circuit diagram of the WPT system is illustrated when

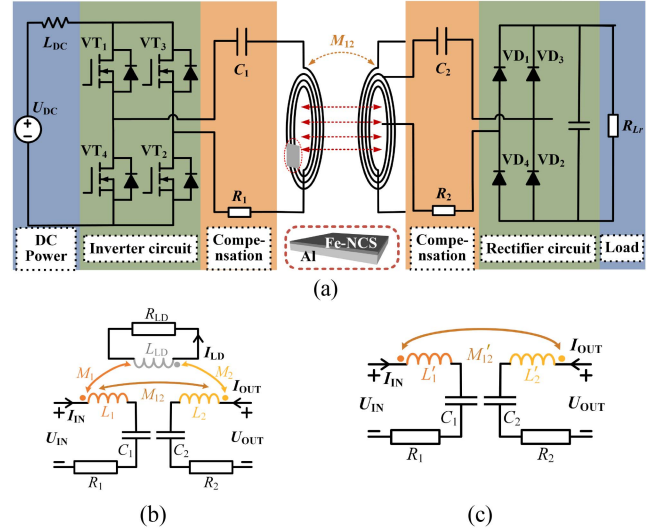


Fig. 2. Circuit model considering levitation device. (a) WPT (intervening the levitation device). (b) Equivalent circuit. (c) Incorporating levitation device effects.

the levitation device is intervened into the system as a metallic material. Fig. 2(c) is the corresponding equivalent circuit diagram after intervening with the levitation device effects into the system.

In [22], the effective self-inductance of the transmitter and receiver is denoted as follows:

$$L'_m = L_m - \omega^2 \frac{M_m^2}{|Z_{LD}|^2} L_{LD} \quad (m = 1, 2). \quad (1)$$

Similarly, the effective mutual inductance with the levitation device can be expressed as follows:

$$M'_{12} = M_{12} - \frac{j\omega M_1 M_2}{Z_{LD}} \quad (2)$$

where $Z_{LD} = R_{LD} + j\omega L_{LD}$.

The levitation device resistance is tens of milliohms for an operating frequency of 10 kHz. In this range, $\omega L_{LD} \gg R_{LD}$. Hence, the effective self-inductances can be further simplified

as follows:

$$L'_m = L_m (1 - k_m^2) \quad (m = 1, 2) \quad (3)$$

where $k_m = M_m / (L_m L_{LD})^{0.5}$ ($m = 1, 2$).

Similarly, the expression of mutual inductance can be simplified as

$$M'_{12} = M_{12} - \frac{M_1 M_2}{L_{LD}} = M_{12} \left(1 - \frac{k_1 k_2}{k_{12}} \right) \quad (4)$$

where $k_{12} = M_{12} / (L_1 L_2)^{0.5}$.

Using these expressions, the effective mutual inductance and the consequent coupling coefficient between the transmitter and receiver is

$$k'_{12} = k_{12} - k_1 k_2. \quad (5)$$

Based on the equation above, the extent of the impact exerted by the levitation device on the WPT system is contingent upon the degree of coupling between the device and the coils.

Upon intervening with the levitation device into the system, the occurrence of eddy currents induced by the device's presence causes changes in the self-inductance of the coils. In addition, the proximity between the levitation device and the coils affects the couplers and alters the mutual inductance within the system. As a consequence, the coupling strength is reduced, leading to modifications in the system power. This phenomenon can be mathematically expressed as follows:

$$\begin{cases} P_{IN} = \text{Re} [\mathbf{U}_{IN} \mathbf{I}_{IN}^*] = \frac{I_{IN}^2 [(\omega M'_{12} b)^2 + R'_1 (R'_2 + R_L) (a^2 + b^2)]}{(a^2 + b^2)(R'_2 + R_L)} \\ P_{OUT} = \text{Re} [\mathbf{I}_{IN} \mathbf{I}_{IN}^* R_L] = \frac{I_{IN}^2 R_L (\omega M'_{12} b)^2 (a^2 + b^2)}{[(a^2 + b^2)(R'_2 + R_L)]^2} \end{cases} \quad (6)$$

where

$$\begin{cases} a = \omega^2 C_2 L'_2 - 1 \\ b = \omega C_2 (R'_2 + R_L) \end{cases}. \quad (7)$$

Through further derivation, the system efficiency can be obtained as follows:

$$\begin{aligned} \eta &= \frac{P_{OUT}}{P_{IN}} \\ &= \frac{(\omega M'_{12} b)^2 R_L}{(R'_2 + R_L) [(\omega M'_{12} b)^2 + R'_1 (R'_2 + R_L) (a^2 + b^2)]}. \end{aligned} \quad (8)$$

In particular, when the levitation device is not present in the system, $a = 0$. In this case, the system power can be as follows:

$$\begin{cases} P_{IN} = \frac{I_{IN}^2 [\omega^2 M'_{12}^2 + R_1 (R_2 + R_L)]}{(R_2 + R_L)} \\ P_{OUT} = \frac{\omega^2 M'_{12}^2 I_{IN}^2 R_L}{(R_2 + R_L)^2}. \end{cases} \quad (9)$$

Similarly, the system efficiency can be as follows:

$$\eta = \frac{\omega^2 M'_{12}^2 R_L}{(R_2 + R_L) [\omega^2 M'_{12}^2 + R_1 (R_2 + R_L)]}. \quad (10)$$

Fig. 3 shows the variations in coil self-inductance and mutual inductance between the coupler for different sizes of the levitation device (positioned centrally at a distance of 30 mm from

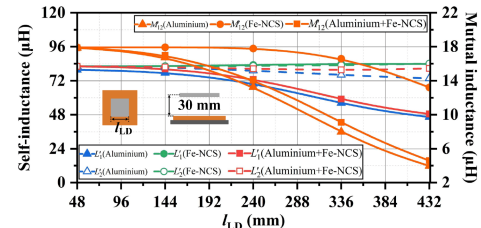


Fig. 3. Effect of levitation device on WPT.

the transmitting coil). As the levitation device's size increases, the coils' self-inductance and the couplers' mutual inductance decrease. The reduction in self-inductance is more pronounced in the transmitting coil than the receiving coil, with the influence of the Fe-NCS being lower than that of the aluminium. In addition, the mutual inductance between the couplers decreases with larger levitation device sizes. However, when the levitation device's side length is less than 72 mm, the coil self-inductance and mutual inductance changes are below 1% and can be considered negligible. Thus, the impact of the levitation device on the system's electrical parameters can be ignored.

Upon intervening with the levitation device, composed of a metallic material, into the system, the self-inductance of the coils undergoes modifications due to the skin effect induced by eddy currents. Furthermore, physical contact or proximity between the levitation device and the coils may decrease coupling strength. Nonetheless, considering the significant difference in size between the levitation device and the coupler, as well as the controlled variations in self-inductance and mutual inductance between the coils and the levitation device during system operation, the impact on energy efficiency parameters is only marginally diminished, remaining within an acceptable range. Notably, this study primarily focuses on optimizing the displacement performance and structure of the levitation device to achieve swift motion and stable levitation. Consequently, within this investigation's scope, the levitation device's influence on energy transfer can be deemed negligible.

The force on the levitation device in the strong electromagnetic coupling environment is analyzed to investigate the functionality of the levitation device. Its motion characteristics in the coupling space are obtained.

A. Force on the Levitation Device

The levitation device in the coupling space can be equivalent to the multiple concentric current rings. Considering the combined effect of induced eddy currents and molecular magnetization currents on the magnetic field, the magnetic flux density near the levitation device can be expressed as

$$\mathbf{B} = \mathbf{B}_0 + \mathbf{B}_e + \mathbf{B}_m = \frac{(1 - \chi_m)^2 B_0}{J_0(kR)} J_0(kr) e_B \quad (11)$$

where r is the equivalent radius of the levitation device. R is the maximum equivalent radius of the levitation device. σ is the electrical conductivity of the aluminium. χ_m is the magnetic susceptibility of the Fe-NCS. μ_0 is the vacuum permeability. \mathbf{B}_0

is the original field strength. J_0 is the zero-order Bessel function, in which

$$k^2 = j\mu_0\sigma\omega \quad (12)$$

where ω is the frequency of the induced eddy current.

In (11), the device's influence on the field strength distribution in the coupling space is considered. And \mathbf{B} is expressed in electromagnetic field theory rather than the traditional analysis based on aggregate circuit theory.

The EMF on the levitation device can be considered as the superposition of the EMFs on the aluminium and the Fe-NCS, which can be derived by

$$\mathbf{F} = \mathbf{F}_J + \mathbf{F}_M. \quad (13)$$

By introducing the magnetic vector potential \mathbf{A}_e , the equivalent eddy current in the aluminium can be derived by

$$\mathbf{J}_e = \nabla \times \mathbf{A}_e = \frac{Bk}{\mu_0 J_0(kR)} J_1(kr) \mathbf{e}_\theta \quad (14)$$

where J_1 is the first-order Bessel function.

The density of EMF per unit volume of the aluminium is

$$\mathbf{f}_e = \mathbf{J}_e \times \mathbf{B} = \frac{B^2 k}{\mu_0 (J_0(kR))^2} J_0(kr) J_1(kr) \mathbf{e}_{\theta \times B}. \quad (15)$$

Taking into account the skin effect of induced eddy currents in thin metal plates, the EMF on the aluminium is

$$\begin{aligned} \mathbf{F}_J &= \int_0^R \mathbf{f}_e dr = \int_0^R \frac{B^2 k}{\mu_0 (J_0(kR))^2} J_0(kr) J_1(kr) \mathbf{e}_{\theta \times B} dr \\ &= \int_S -\frac{B^2}{2\mu_0} \left(1 - \frac{1}{(J_0(kR))^2} \right) \mathbf{e}_{\theta \times B} dS \\ &= K_e \int_S \frac{B^2}{2\mu_0} \mathbf{e}_{\theta \times B} dS \propto K_e \frac{B^2}{2\mu_0} \mathbf{e}_{\theta \times B}. \end{aligned} \quad (16)$$

Based on (16), the EMF on the aluminium obeys the left-hand rule, and the behavior of the overall force is the repulsion of the adjacent side coupler. The force's amplitude is related to the material properties and dimensions of the aluminium and the magnetic flux density. The influence factor K_e is specified to represent the contribution of the material properties and dimensions of the aluminium to the force.

According to the Maxwell's stress method, the EMF density per unit surface area of the Fe-NCS is expressed as

$$\mathbf{f}_m = \frac{1}{\mu_0} (\mathbf{n} \cdot \mathbf{B}) \mathbf{B} - \frac{1}{2\mu_0} B^2 \mathbf{n} \quad (17)$$

where \mathbf{n} is the normal unit vector of the Fe-NCS.

The EMF on the Fe-NCS can be derived by

$$\begin{aligned} \mathbf{F}_M &= \int_S \mathbf{f}_m dS = \int_S \left(\frac{1}{\mu_0} (\mathbf{n} \cdot \mathbf{B}) \mathbf{B} - \frac{1}{2\mu_0} B^2 \mathbf{n} \right) dS \\ &= \int_S \frac{1}{2\mu_0 (1 + \chi_m)^2} B^2 \mathbf{n} dS = K_m \int_S \frac{B^2}{2\mu_0} \mathbf{n} dS \propto K_m \frac{B^2}{2\mu_0} \mathbf{n}. \end{aligned} \quad (18)$$

TABLE I
PARAMETERS OF THE WPT SYSTEMS

Symbol	PARAMETER	Value
I_{IN}	The RMS current in the transmitter coil	100 A
f	Resonance frequency	10 kHz
R_{Lr}	Load resistance	9 Ω
R_l	Equivalent resistance of the coil branch	0.1 Ω
M_{12}	Mutual inductance between the transmitter and receiver coils	18.22 μH

Based on (18), the EMF and the magnetic flux density of the Fe-NCS are in the same direction. The behavior of the overall force is the attraction of the adjacent side coupler. The force's amplitude is related to the material properties, dimensions, and magnetic flux density. The influence factor K_m is specified to represent the contribution of the material properties and dimensions of the Fe-NCS to the force.

The standard sinusoidal expression for the magnetic induction intensity in the coupling space of a WPT system is represented as follows:

$$B(t) = \sqrt{2}B \sin(\omega t + \varphi_B). \quad (19)$$

Upon substituting the standard sinusoidal expression for the magnetic induction intensity, the equation can be obtained as follows:

$$\begin{cases} F_J \propto K_e \left[\frac{1}{\mu_0} B^2 - \frac{1}{\mu_0} B^2 \cos(2\omega t + 2\varphi_B) \right] \\ F_M \propto K_m \left[\frac{1}{\mu_0} B^2 - \frac{1}{\mu_0} B^2 \cos(2\omega t + 2\varphi_B) \right]. \end{cases} \quad (20)$$

The force exerted on the levitation device is inherently linked to the system frequency. The EMF acting upon the levitation device exhibits a periodic nature, oscillating twice that of the system's operational frequency.

The forces on the aluminium and the Fe-NCS are analyzed. Fig. 1 shows the model diagram of the WPT system. The transmitting coil flows 100-A current, and the compensation topology of the system is SS type. The specific parameters of the WPT system are shown in Table I. The initial positions of the aluminium and the Fe-NCS are specified, and its geometric centre is 30-mm away from the surface of the transmitter coil and located in the center of the unilateral coupled coils.

Fig. 4 shows the waveforms of the EMFs on the aluminium and the Fe-NCS, where the aluminium and the Fe-NCS have the same size ($50 \times 50 \times 2$ mm 3), and the direction of the force on the aluminium is specified as the positive direction. The force on the aluminium is a periodic electromagnetic repulsion force with an amplitude of 1.56 N along the y -axis. The force on the Fe-NCS is a periodic electromagnetic attraction force with an amplitude of 0.46 N along the y -axis. Along the x -axis, the force on the aluminium is a periodic EMF with an amplitude of 14 mN, which is the same as its phase along the y -axis. The force along the x -axis of the Fe-NCS is similar to that of the aluminium, and the amplitude of the EMF is 3.4 mN. The EMFs on the aluminium and the Fe-NCS have the same period, and the direction of the force is opposite at any time.

According to Fig. 4, the forces acting on the aluminium and the Fe-NCS in the coupling space of the WPT system

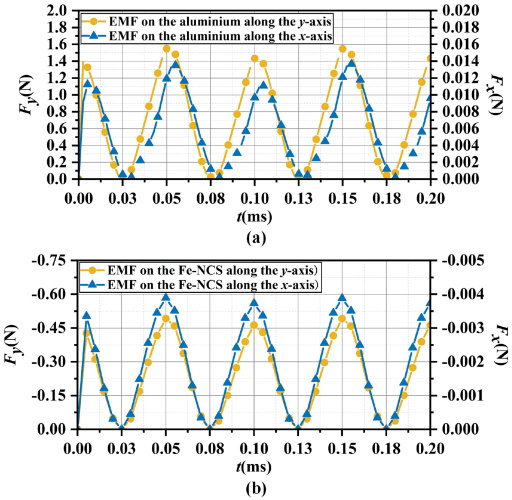


Fig. 4. EMFs on the aluminium and the Fe-NCS. (a) Aluminium. (b) Fe-NCS.

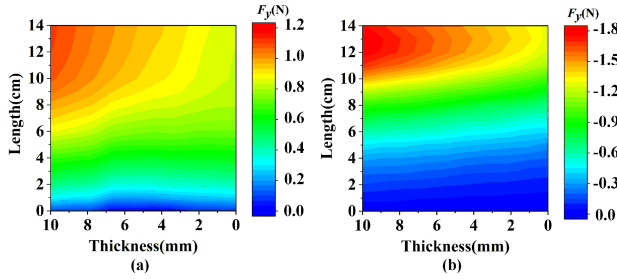


Fig. 5. EMF on the aluminium and the Fe-NCS under different dimensions. (a) Aluminium. (b) Fe-NCS.

exhibit complementary characteristics. The aluminium experiences electromagnetic repulsion, supporting levitation and enabling fast lateral movement of the device. However, it should be noted that the dominant electromagnetic repulsion compromises the stable levitation state. To mitigate this, the introduction of electromagnetic attraction acting on the Fe-NCS is considered, which counteracts the repulsion and maintains the levitation state. The optimization of the device's structure becomes essential to address the challenge of destabilization caused by the introduction of electromagnetic attraction.

According to the previous analysis, the dimensions affect the forces on the aluminium and the Fe-NCS. Fig. 5 shows the variations of the steady-state components of the EMF along the y-axis on the aluminium and the Fe-NCS under different dimensions. At the same thickness, the forces on both the aluminium and the Fe-NCS increase with their length. At the same length, the forces on both the aluminium and the Fe-NCS increase as the thickness increases, verifying the correctness of (16) and (18). Therefore, with the increasing dimensions of the material, the electromagnetic field has a stronger effect on its EMF.

As analyzed above, the EMF on the levitation device of the WPT system relates to the material properties and dimensions, which have a positive correlation with the magnetic flux density.

The levitation device in the WPT system is composed of aluminium and Fe-NCS, exhibiting different force characteristics

TABLE II
DYNAMIC MODEL PARAMETERS OF THE LEVITATION DEVICE

Symbol	Parameter	Value
ρ_{Nc}	Density of the Fe-NCS	7.18 g/cm ³
ρ_{Al}	Density of the aluminium	2.70 g/cm ³
C	Wind resistance coefficient	1
μ_f	Sliding friction coefficient	0.3

within the WPT system. Combining the EMFs of these two materials achieves stable levitation and horizontal displacement motion of the device. Notably, the proposed driving method for the microdisplacement device in the WPT system enables self-induced motion without relying on sensor feedback. Instead, it leverages the electromagnetic environment to drive the device. The stable levitation relies on the balance between gravity and electromagnetic repulsion, resulting in a sustained oscillatory equilibrium state.

B. Motion Characteristics of the Levitation Device

The levitation device is subjected to the EMF to generate regular motion between the coupling area of the WPT system, and its dynamic characteristics are closely related to the electromagnetic field distribution characteristics. During the overall motion, the electromagnetic energy and mechanical energy are transformed into each other. Assuming the mass of the levitation device is m . The dynamic motion of the levitation device can be modeled by

$$\begin{cases} m \frac{d^2x}{dt^2} = F_x - C_x S_x \left(\frac{dx}{dt} \right)^2 - k \mu_f (F_y - mg) \\ m \frac{d^2y}{dt^2} = F_y - C_y S_y \left(\frac{dy}{dt} \right)^2 - mg \end{cases} \quad (21)$$

where $F_{(i)}$, $C_{(i)}$, and $S_{(i)}$ are the components of the EMF, the wind resistance coefficients, and the levitation device's windward areas, respectively. i refers to the x - and y -directions. μ_f is the sliding friction factor, and k is the sliding friction condition factor. $k = 1$ means that the levitation device is in contact with the surface of the receiver coil, $k = -1$ means that the levitation device is in contact with the surface of the transmitter coil. Otherwise, $k = 0$.

Based on (21), the motion state of the levitation device relates to the spatial field strength distribution between the coupled coils of the WPT system and its material properties and dimensions. The steady-state position of the levitation device in the vertical direction is determined by the difference between its weight and the y -component of the EMF. When the difference is zero, the levitation device is stably levitated. The x -component of the EMF provides the driving force for the levitation device, which drives it to generate horizontal displacement motion.

To simplify the analyze, the thickness of the levitation device is set to be fixed, where the thicknesses of the aluminium and the Fe-NCS are 2 and 0.25 mm, respectively. The levitation device is a vertical plane body whose drag coefficient satisfies $C = C_x = C_y = 1$. The densities of the aluminium and the Fe-NCS are 2.70 and 7.18 g/cm³, respectively, and their weights obey $m = \rho v$. Table II shows the dynamic model parameters of the levitation.

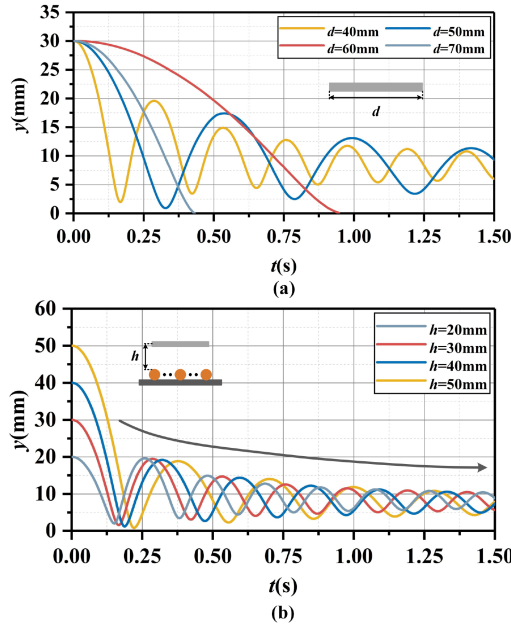


Fig. 6. Vertical motion characteristics of the levitation device. (a) Different dimensions. (b) Different initial heights.

The initial position of the levitation device is the same as that described in Section II-A. The initial position of the levitation device is shown in Fig. 1. The levitation device is driven by the EMF. The motion of the levitation device is decomposed into the vertical and horizontal motions. Its initial position is defined as the origin, where $x = 0$ and $y = 0$.

Fig. 6 shows the vertical motion characteristics of the levitation device. As shown in Fig. 6(a), the levitation device acts as damping vibration in the vertical direction. When the length of the levitation device is 60 and 70 mm, the vertical displacement of the levitation device acts as the overdamping characteristics, and the levitation device reaches the steady state at 0.93 and 0.42 s, respectively. When the length of the levitation device is 40 and 50 mm, the vertical displacement of the levitation device performs as the underdamping characteristics. It reaches the steady state at 0.65 and 1.22 s, respectively. Its steady-state heights are 8.97 and 7.45 mm, respectively. Fig. 6(b) shows the vertical displacement of the levitation device under different initial heights. The final steady-state height of the levitation device is 8.97 mm, while the length of the levitation device is 40 mm. As the initial height increases, the levitation device takes longer to stabilize.

Fig. 7 shows the motion characteristics of the levitation device in the horizontal direction. The levitation device performs as a forward driving motion in the horizontal direction. To analyze the Fe-NCS contribution to the levitation device's horizontal motion, a comparison between the fully coated Fe-NCS structure and the uncoated Fe-NCS structure is made under the length of 40 mm. The average horizontal velocity of the levitation device with the fully coated Fe-NCS structure is greater than that of the levitation device without the Fe-NCS structure in any period. The Fe-NCS coating can improve the horizontal dynamic response of the levitation device.

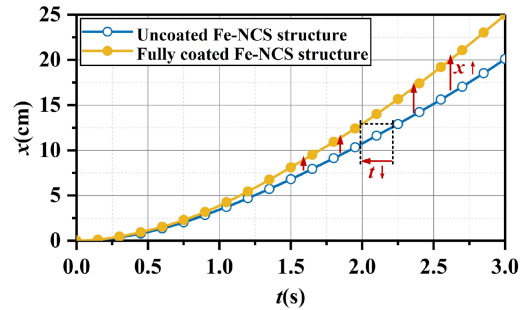


Fig. 7. Horizontal motion characteristics of the levitation device.

For the levitation device of the WPT system, its dynamic characteristics relate to the dimensions and composition of the materials. The force on the aluminium provides a stable levitation contribution to the levitation device, and the force on the Fe-NCS can further improve the horizontal dynamic characteristics of the levitation device.

This section analyzes the force and motion characteristics of the levitation device. In the horizontal direction, the device experiences two types of EMFs that act in opposite directions. The electromagnetic repulsive force acting on the metal primarily contributes to the lateral displacement of the device. However, it is essential to note that the electromagnetic repulsive force compromises the suspension state of the device. To address this, we introduce the attractive EMF experienced by Fe-NCS. Due to the higher EMF on aluminium compared to Fe-NCS for the same volume, the lateral motion characteristics of the device predominantly rely on the repulsive EMF. In addition, in the vertical direction, the repulsive EMF is counteracted by the attractive EMF and the weight, maintaining the levitation state of the device. Overall, including Fe-NCS enhances the levitation device's lateral dynamic characteristics.

III. OPTIMIZATION OF DYNAMIC CHARACTERISTICS OF THE LEVITATION DEVICE WITH THE GRID-TYPE FE-NCS STRUCTURE

According to Section I, the motion state of the levitation device consisting of the Fe-NCS and the aluminium relates to its structure. The aluminium is mainly affected by electromagnetic repulsion, which provides the levitation device with levitation support. At the same time, it provides the driving force for the levitation device together with the Fe-NCS. The Fe-NCS are affected by electromagnetic attraction, which will affect the vertical steady state of the levitation device. To stabilize the levitation device and provide the driving force required for rapid movement, this article proposes a levitation device with the grid-type Fe-NCS structure, as shown in Fig. 1. The thin layer of grid-type Fe-NCS strip is uniformly attached to the surface of the aluminium sheet.

A. Optimization Objectives for Dynamic Characteristics

To achieve stable levitation and rapid moving motion, the grid-type Fe-NCS structure should be optimized. The number and

width of the grid strips are optimized to adjust the contribution of the driving force of different materials to obtain the best dynamic characteristics.

The optimization objectives and constraints can be expressed as

$$\begin{aligned} \text{maximize : } v_{\text{xav}} &= \frac{x_o}{t_{ld}} \\ \text{subject to : } h_s &> 0 \\ 0 \leq N &\leq N_{\max} \\ 0 \leq W &\leq LN^{-1} \\ x_n &= x_0 + \frac{D(2n-1)}{2N} \quad (n = 1, 2, \dots, N_{\max}) \end{aligned} \quad (22)$$

where W and L are the width and length of the grid-type Fe-NCS strip, respectively, N is the number of grid-type Fe-NCS strips, and its value is an integer. N_{\max} is the maximum number of grid-type Fe-NCS strips. $x_n - x_0$ is the distance between the n th and the side-most grid-type Fe-NCS strips. D is the length of the aluminium. v_{xav} is the average horizontal velocity of the levitation device. To evaluate the horizontal motion characteristics of the levitation device, the length of the horizontal motion observation zone is set to be 25 cm. h_s is the minimum oscillation distance between the levitation device and the surface of the transmitter coil.

The mathematical model function for the optimization objective consists of two distinct components: 1) characterizing the levitation device's dynamic behavior and 2) the imposition of size constraints. Specifically, the average lateral velocity of the levitation device is represented by v_{xav} , and the condition $h_s > 0$ indicates the achievement of a stable levitated state. The constraints N and W are associated with the geometric limitations imposed on the grid-type Fe-NCS structure. At the same time, x_n ensures the uniform distribution of the grid-type Fe-NCS on the surface of the aluminium substrate.

B. VA-PSO Algorithm

The PSO algorithm is based on group behavior, which obtains the optimal global solution by simulating a flock of birds foraging [20]. In which a particle represents the individuals in the flock, it only has velocity and acceleration. The group consisting of particles independent of each other is called the particle swarm. The group converges to the unique food location by updating the individual position [21]. The PSO is selected for optimizing the structure of the levitation device due to its strong convergence properties in handling multiobjective optimization problems.

Assume that the group consists of N_g independent particles and the optimization is carried out in a specific space of M dimensions. The position of the i th particle in the j th dimension is x_{ij} , and its velocity is v_{ij} . The optimal position of the i th particle in the j th dimension during the solution process is pb_{ij} . The state equation

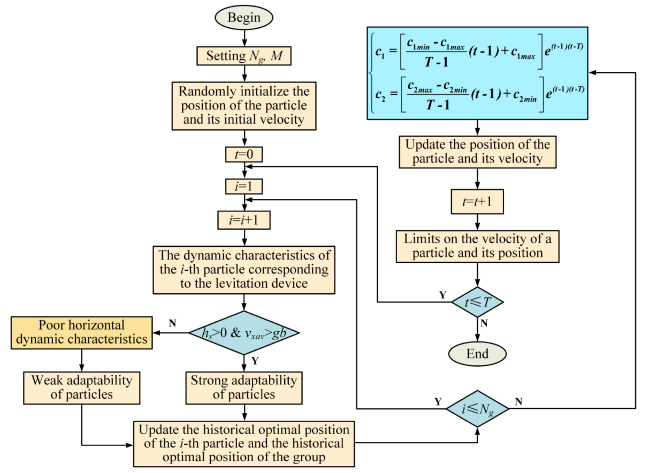


Fig. 8. Optimization flowchart of the dynamic characteristic of the levitation device based on the VA-PSO algorithm.

of the i th particle in the j th dimension at the t th iteration is

$$\begin{cases} x_{ij}(t+1) = x_{ij}(t) + v_{ij}(t+1) \\ v_{ij}(t+1) = \omega_i v_{ij}(t) + c_1 r_1 (pb_{ij} - x_{ij}(t)) \\ \quad + c_2 r_2 (gb - x_{ij}(t)) \\ 1 \ll i \ll N_g \\ 1 \ll j \ll M. \end{cases} \quad (23)$$

The above equation is the standard PSO algorithm equation. ω_i is the inertia weight coefficient, and the larger its value, the stronger the local search ability of the group. The acceleration coefficients c_1 and c_2 represent the self-learning ability and the social learning ability of independent particles, respectively. Initially, to obtain a large-scale search ability and avoid falling into the local optimal solution, the value of c_1 should be sufficiently large, and the value of c_2 should be sufficiently small. On the contrary, when it is at the end of the solution optimization, the value of c_2 should be sufficiently large, and the value of c_1 should be sufficient to improve the convergence speed of the solution. Therefore, this article proposes the VA-PSO algorithm, where the acceleration coefficient at the t th iteration is

$$\begin{cases} c_1 = \left[\frac{c_{1\min} - c_{1\max}}{T-1} (t-1) + c_{1\max} \right] e^{(t-1)(t-T)} \\ c_2 = \left[\frac{c_{2\max} - c_{2\min}}{T-1} (t-1) + c_{2\min} \right] e^{(t-1)(t-T)} \end{cases} \quad (24)$$

where T is the total number of the optimization iterations. $c_{i\min}$ ($i = 1, 2$) and $c_{i\max}$ ($i = 1, 2$) are the upper and lower limits of the acceleration coefficients.

The proposed VA-PSO algorithm is an asynchronous learning factor-based PSO method that combines extensive exploration in the initial phase with accelerated convergence in the final phase.

C. Optimization of the Dynamic Characteristics of the Levitation Device

The optimization flowchart of the dynamic characteristic of the levitation device based on the VA-PSO algorithm is shown in Fig. 8. The VA-PSO algorithm is improved by adjusting the acceleration coefficients in the iterative process, satisfying

TABLE III
PARAMETERS OF THE VA-PSO ALGORITHM

Symbol	Parameter	Value
D	Length of the aluminium mm	60
N_{\max}	Maximum number of the grid strips	4
N_g	Size of particle swarm	14
ω_i	Inertia weight coefficient	0.73
c_{\min} ($i=1,2$)	Upper limits of the acceleration coefficients	2.53
c_{\max} ($i=1,2$)	Lower limits of the acceleration coefficients	1.78
T	Total number of the optimization iterations	40

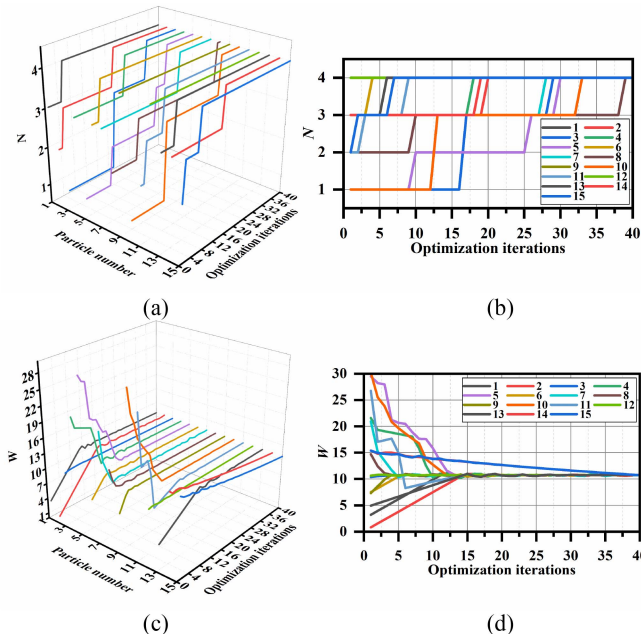


Fig. 9. Parameter optimization based on the VA-PSO algorithm. (a) Number of grid strips (3-D). (b) Number of grid strips (2-D). (c) Width of grid strips (3-D). (d) Width of grid strips (2-D).

the requirements of the acceleration coefficient under different iteration stages.

The particles in the group are initialized through random position distribution. The adaptability of the independent particles is numerically resolved. Their velocities and positions are updated by learning their optimal historical positions till the group approaches the optimal solution position. Table III shows the parameters of the VA-PSO algorithm.

Based on the VA-PSO algorithm, the optimization of the dynamic characteristics of the levitation device with the grid-type Fe-NCS structure is presented in Fig. 9. As the optimization iterations proceed, the number and width of the grid strips approach the optimal solution position and are stabilized after 20 iterations, i.e., $N = 4$, $W = 10.7$ mm. The optimization results show that the number of grid strips tends to the maximum within the specified range. In practical applications, the number of strips should be limited due to engineering conditions.

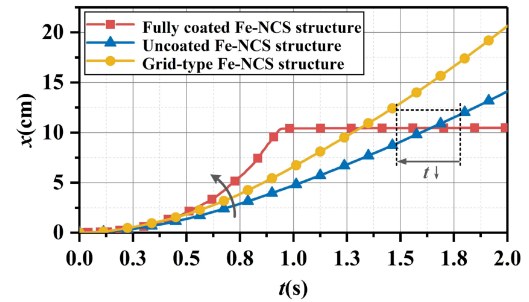


Fig. 10. Horizontal motion characteristics of the levitation device with the grid-type Fe-NCS structure.

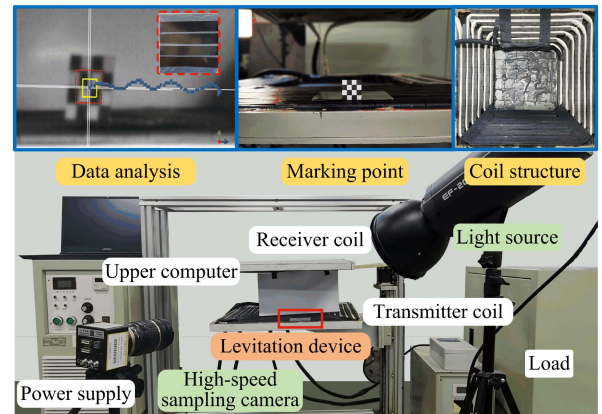


Fig. 11. Prototype for motion characteristics of the levitation device.

The horizontal motion characteristics of the optimized levitation device are illustrated in Fig. 10. The levitation device with the fully coated Fe-NCS structure cannot be levitated stably in the vertical direction. Its maximum horizontal displacement distance is 10.4 cm. Compared to the levitation device without the grid-type Fe-NCS structure, the time taken for the levitation device with the grid-type Fe-NCS structure to pass through the horizontal displacement of 12 cm is decreased from 1.78 to 1.43 s. The average horizontal velocity increases by 18.5%.

Based on the above analysis, the levitation device with the grid-type Fe-NCS structure optimized by the VA-PSO algorithm avoids the inability to maintain the vertical levitate stably under the condition of fully coated Fe-NCS. At the same time, it has the characteristics of rapid displacement in the horizontal direction.

IV. VERIFICATION EXPERIMENTS FOR OPTIMIZATION OF DYNAMIC CHARACTERISTICS OF THE LEVITATION DEVICE

A 3.7-kW WPT prototype with the levitation device is built to validate the proposed design and analysis, as shown in Fig. 11. The parameters of the WPT system are the same as that described in Section I. The motion states of the marked levitation devices with different dimensions and structures are obtained by using the high-speed sampling camera. The collected motion trajectory data of the levitation drive are analyzed by the upper computer.

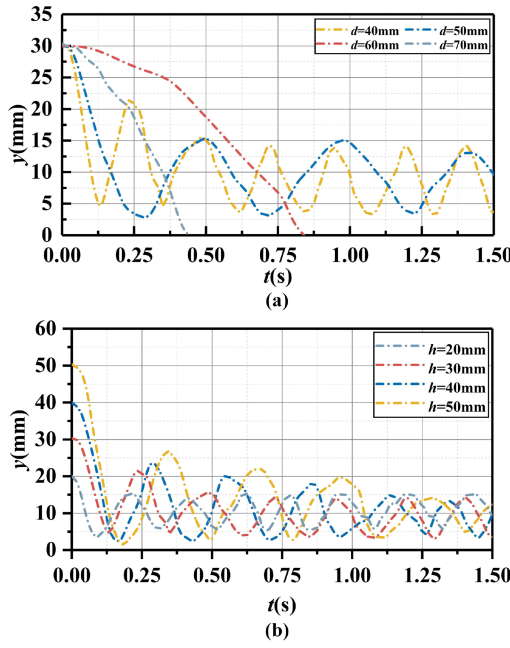


Fig. 12. Vertical motion characteristics of the levitation device under different conditions. (a) Different dimensions. (b) Different initial heights.

Based on the discussion in Section II-A regarding the force exerted on the levitation device, it is evident that the EMF acting on the device exhibits periodic behavior with a vibration frequency that is twice the system's operating frequency. However, as outlined in Section II-B, concerning the motion characteristics of the levitation device, the ultimate motion state of the device is determined by the magnitude of the EMF. Therefore, the choice of the system frequency is relatively independent of the focus of this article. Considering the widespread adoption of low frequencies, such as 10 kHz, in practical applications, the selection of 10 kHz as the system's operating frequency in this article is based on previous research experiences and successful real-world implementations.

The vertical motion characteristics of the levitation device with the fully coated Fe-NCS structure are shown in Fig. 12. Set the initial height of the levitation device as $h = 30. The vertical motion characteristics are compared under different dimensions conditions. When the length of the levitation device is 40 and 50 mm, the vertical motion trajectories perform as the underdamping oscillation, which has the steady-state levitation heights of 8.8 and 8.45 mm reached at 0.63 and 1.21 s, respectively. When the length of the levitation device is 60 and 70 mm, the vertical motion trajectories perform as the overdamping oscillation, and the steady states are obtained at 0.38 and 0.84 s, respectively. The vertical motion characteristics of the levitation device with the fully coated Fe-NCS structure versus the initial height under the same length of 40 mm are compared in Fig. 12(b). The results show that the final steady-state levitation height is 8.8 cm, which is independent of the initial height. However, the time for the levitation device to reach the steady state increases with the increase of the initial height. When the length of the levitation device is 20 and$

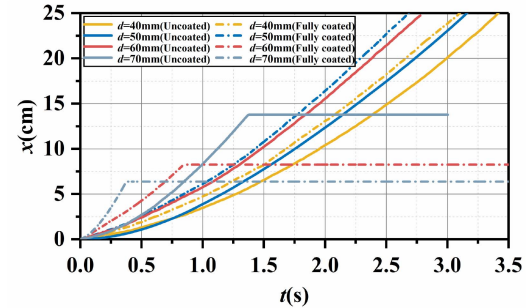


Fig. 13. Horizontal motion characteristics of the levitation device under different structures.

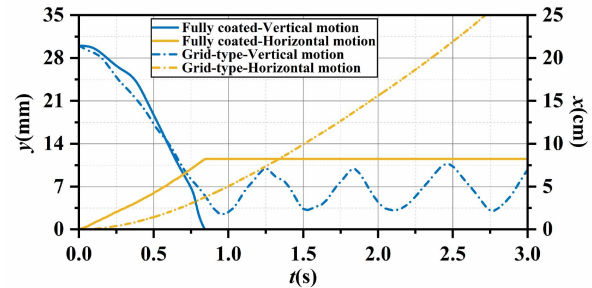


Fig. 14. Motion characteristics of the levitation device ($L = D = 60).$

50 mm, the stable levitations are reached at 0.53 and 1.12 s, respectively.

The horizontal trajectory of the levitation device with and without the fully coated Fe-NCS structure is compared in Fig. 13. The Fe-NCS coating can improve the horizontal dynamic response of the levitation device. When the length of the levitation device is 40 mm, the average horizontal velocity is 7.4 cm/s under the condition that the Fe-NCS are not coated. After the Fe-NCS is fully coated, the average horizontal velocity increases by 9.46% to 8.1 cm/s. When the length of the levitation device is 70 mm, the levitation device with and without the fully coated Fe-NCS structure reaches the steady state at 0.38 and 1.31 s, respectively. The levitation device cannot reach steady-state levitation when the length of the levitation device with the fully coated Fe-NCS structure is 60 mm, which is consistent with the simulation results.

To solve the problem that the levitation device with the fully coated Fe-NCS structure cannot maintain stable levitation under the condition of large size, the grid-type Fe-NCS structure is proposed and optimized by the VA-PSO algorithm. The levitation device with a length of 60 mm is taken as the optimization objective.

The comparison of the motion trajectory of the levitation device with the fully coated Fe-NCS structure and with the grid-type Fe-NCS structure is presented in Fig. 14. Due to the electromagnetic attraction, the vertical motion of the levitation device with the fully coated Fe-NCS structure cannot maintain a stable levitation when the length is 60 mm. The optimized levitation device with the grid-type Fe-NCS structure can achieve stable levitation and rapid horizontal displacement.

It reaches an oscillation levitation state at 0.97 s, and its stable levitation height is 6.5 mm. With the grid-type Fe-NCS structure, the average horizontal velocity increases by 22.3% to 9.3 cm/s compared to the levitation device without the Fe-NCS structure. The experimental results are consistent with the simulation results and prove the accuracy of the optimization results. The system efficiency demonstrates fluctuations within the 85% to 89% range, demonstrating its ability to maintain a relatively high energy transfer efficiency within a defined operational range.

The discrepancy between the experimental and simulation results can be attributed to two main factors. First, in the simulation, the levitation device is assumed to experience balanced air resistance solely in the vertical direction. At the same time, in actual experiments, its slight inclination introduces additional air resistance in the horizontal direction. Although this inclination has a negligible effect on the device's motion characteristics, it contributes to the observed differences. Second, the accuracy of the experimental results is influenced by the inherent limitations and measurement errors of the high-speed camera used for data acquisition.

V. CONCLUSION

To drive the levitation device and realize power transfer at the same time in the WPT system, a levitation device consisting of the aluminium and the Fe-NCS is proposed based on the performance of the EMF on the two materials. The Fe-NCS can enhance the horizontal dynamic response of the levitation device but is harmful to the levitation device's vertical steady state. To solve the problem that the levitation device with the fully coated Fe-NCS structure cannot maintain the steady-state levitation under large size, the grid-type Fe-NCS structure is proposed and optimized by using VA-PSO algorithm, achieving the stable vertical levitation and rapid horizontal displacement. A 3.7-kW prototype is built to verify the proposed design. The optimized levitation device with the grid-type Fe-NCS structure can achieve stable vertical levitation at 0.97 s with an average horizontal velocity of 9.3 cm/s.

REFERENCES

- [1] A. P. Sample, D. A. Meyer, and J. R. Smith, "Analysis, experimental results, and range adaptation of magnetically coupled resonators for wireless power transfer," *IEEE Trans. Ind. Electron.*, vol. 58, no. 2, pp. 544–554, Feb. 2011.
- [2] S. Y. R. Hui, W. Zhong, and C. K. Lee, "A critical review of recent progress in mid-range wireless power transfer," *IEEE Trans. Power Electron.*, vol. 29, no. 9, pp. 4500–4511, Sep. 2014.
- [3] Z. Yuan, M. Saeedifard, C. Cai, Q. Yang, P. Zhang, and H. Lin, "A misalignment tolerant design for a dual-coupled LCC-S-compensated WPT system with load-independent CC output," *IEEE Trans. Power Electron.*, vol. 37, no. 6, pp. 7480–7492, Jun. 2022.
- [4] X. Dai, X. Li, Y. Li, and A. P. Hu, "Maximum efficiency tracking for wireless power transfer systems with dynamic coupling coefficient estimation," *IEEE Trans. Power Electron.*, vol. 33, no. 6, pp. 5005–5015, Jun. 2018.
- [5] R. Mai, Y. Liu, Y. Li, P. Yue, G. Cao, and Z. He, "An active-rectifier-based maximum efficiency tracking method using an additional measurement coil for wireless power transfer," *IEEE Trans. Power Electron.*, vol. 33, no. 1, pp. 716–728, Jan. 2018.
- [6] W. Han, K. T. Chau, C. Jiang, W. Liu, and W. H. Lam, "Design and analysis of quasi-omnidirectional dynamic wireless power transfer for fly-and-charge," *IEEE Trans. Magn.*, vol. 55, no. 7, Jul. 2019, Art. no. 8001709.
- [7] P. Zhang, M. Saeedifard, O. C. Onar, Q. Yang, and C. Cai, "A field enhancement integration design featuring misalignment tolerance for wireless EV charging using LCL topology," *IEEE Trans. Power Electron.*, vol. 36, no. 4, pp. 3852–3867, Apr. 2021.
- [8] P. Zhang et al., "WPT-based voltage equalizer for scalable cell-string charging," *IEEE Trans. Ind. Electron.*, vol. 71, no. 1, pp. 493–503, Jan. 2024.
- [9] F. Lin, S. Zuo, W. Deng, and S. Wu, "Modeling and analysis of electromagnetic force, vibration, and noise in permanent-magnet synchronous motor considering current harmonics," *IEEE Trans. Ind. Electron.*, vol. 63, no. 12, pp. 7455–7466, Dec. 2016.
- [10] D. Rus and M. T. Tolley, "Design, fabrication and control of origami robots," *Nature Rev. Materials*, vol. 3, no. 6, pp. 101–112, 2018.
- [11] H. Lu et al., "A bioinspired multilegged soft millirobot that functions in both dry and wet conditions," *Nature Commun.*, vol. 9, no. 1, 2018, Art. no. 3944.
- [12] D. Kim, K. Hwang, J. Park, H. H. Park, and S. Ahn, "High efficiency wireless power and force transfer for micro-robot using 3-axis AC/DC magnetic coil," in *Proc. 17th IEEE Biennial Conf. Electromagn. Field Computation*, 2016, pp. 14–18.
- [13] D. Kim, J. Park, K. Kim, H. H. Park, and S. Ahn, "Propulsion and control of implantable micro-robot based on wireless power transfer," in *Proc. IEEE Wireless Power Transfer Conf.*, 2015, pp. 1–4.
- [14] D. Kim, M. Kim, J. Yoo, H. H. Park, and S. Ahn, "Magnetic resonant wireless power transfer for propulsion of implantable micro-robot," *J. Appl. Phys.*, vol. 117, no. 17, 2015, Art. no. 17E712.
- [15] K. Oka and M. Tanaka, "A simple levitation system using wireless power supply system and Lorentz force," *J. Phys. Conf. Ser.*, vol. 744, no. 1, 2016, Art. no. 12233.
- [16] M. Liu, K. W. Chan, J. Hu, Q. Lin, J. Liu, and W. Xu, "Design and realization of a coreless and magnetless electric motor using magnetic resonant coupling technology," *IEEE Trans. Energy Convers.*, vol. 34, no. 3, pp. 1200–1212, Sep. 2019.
- [17] F. Wang et al., "Electromagnetic force suppression of the coupling mechanism structure of WPT system based on phase difference control," *Trans. China Electrotechnical Soc.*, vol. 37, no. 1, pp. 141–151, 2021.
- [18] X. Hao, I. Salhi, S. Laghrouche, Y. Ait-Amirat, and A. Djerdir, "Backstepping supertwisting control of four-phase interleaved boost converter for PEM fuel cell," *IEEE Trans. Power Electron.*, vol. 37, no. 7, pp. 7858–7870, Jul. 2022.
- [19] X. Yang, Q. Huang, S. Jing, M. Zhang, Z. Zuo, and S. Wang, "Servo system control of satcom on the move based on improved ADRC controller," *Energy Rep.*, vol. 8, pp. 1062–1070, 2022.
- [20] T. Xu, J. Zhang, M. Salehizadeh, O. Onaizah, and E. Diller, "Millimeter-scale flexible robots with programmable three-dimensional magnetization and motions," *Sci. Robot.*, vol. 4, no. 29, 2019, Art. no. v4494.
- [21] S. Miyashita, S. Guitron, S. Li, and D. Rus, "Robotic metamorphosis by origami exoskeletons," *Sci. Robot.*, vol. 2, no. 10, 2017, Art. no. o4369.
- [22] M. Mohammad, E. T. Wodajo, S. Choi, and M. E. Elbuluk, "Modeling and design of passive shield to limit EMF emission and to minimize shield loss in unipolar wireless charging system for EV," *IEEE Trans. Power Electron.*, vol. 34, no. 12, pp. 12235–12245, Dec. 2019.



Fengxian Wang received the B.S. degree in electrical engineering and the M.S. degree in electrical engineering from Tiangong University, Tianjin, China, in 2018 and 2021, respectively. He is currently working toward the Ph.D degree in electrical engineering with the Hebei University of Technology, Tianjin, China.

His research interests include engineering electromagnetism, wireless power transfer, and its industrial applications.



Qingxin Yang received the B.S., M.S., and Ph.D. degrees in electrical engineering from the Hebei University of Technology, Tianjin, China, in 1983, 1986, and 1997, respectively.

Since 1996, he has been a Professor with the Hebei University of Technology. From 2008 to 2018, he was the President of Tianjin Polytechnic University, Tianjin, China. From 2018 to 2020, he was the President of the Tianjin University of Technology, Tianjin, China. His research interests include computational electromagnetism, engineering electromagnetism and their applications, and special wireless power transfer.

Dr. Yang was a Board Member of International COMPUMAG Society and the President of China chapter. Since 2015, he has been the President of China Electrotechnical Society.



Zhaoyang Yuan (Member, IEEE) received the B.S. degree in electrical engineering and the M.S. degree in control science and engineering from Tiangong University, Tianjin, China, in 2015 and 2018, respectively. He is currently working toward the Ph.D. degree in electrical engineering with Hebei University of Technology, Tianjin, China.

From October 2019 to October 2021, he was a Visiting Researcher with the School of Electrical and Computer Engineering, Georgia Institute of Technology, Atlanta, GA, USA. His research interests

include engineering electromagnetism, wireless power transfer, and its industrial applications.



Xian Zhang received the M.E., and Ph.D. degrees in electrical engineering from the Hebei University of Technology, Tianjin, China, in 2009, and 2012, respectively.

He is currently a Professor with the Hebei University of Technology, Tianjin, China. His research interests include intelligent high-power wireless power transmission technology, measurement of 3-D electromagnetic fields, and numerical calculations of modern engineering electromagnetic fields.

Dr. Zhang is the Director of the China Electrotechnical Society and the Secretary-General of the National Specialized Committee on Wireless Power Transmission Technology.



Xuejing Ni was born in Heilongjiang, China, in 1996. She received the B.S. degree in electrical engineering from the Department of Electrical Engineering, North China University of Water Resources and Electric Power, Zhengzhou, China, in 2016, and the M.S. degree in electrical engineering from the Department of Electrical Engineering, Tiangong University, Tianjin, China, in 2020.

She is currently an Electrical Engineer with the GD Power Shuangwei Inner Mongolia Shanghai-miao Energy Company, Ltd. Her research interests include engineering electromagnetism, wireless power transfer, and its industrial applications.